# 3D Fluid Simulations of Tokamak Edge Turbulence

A. Zeiler and D. Biskamp;
J.F. Drake and P.N. Guzdar

IPP 6/333

September 1995


MAX-PLANCK-INSTITUT FÜR PLASMAPHYSIK

85748 GARCHING BEI MÜNCHEN

MAX-PLANCK-INSTITUT FÜR PLASMAPHYSIK

GARCHING BEI MÜNCHEN

# 3D Fluid Simulations of Tokamak Edge Turbulence

A. Zeiler and D. Biskamp
Max-Planck-Institut für Plasmaphysik,
EURATOM Association, 85748 Garching, Germany

J. F. Drake and P. N. Guzdar
Institute for Plasma Research, University of Maryland
College Park, Maryland, 20742, USA

**Abstract**

3D simulations of drift resistive ballooning turbulence are presented. The turbulence is basically controlled by a parameter $\alpha$, the ratio of the drift wave frequency to the ideal ballooning growth rate. If this parameter is small ($\alpha \leq 1$, corresponding to Ohmic or L-mode plasmas), the system is dominated by ballooning turbulence, which is strongly peaked at the outside of the torus. If it is large ($\alpha \geq 1$, corresponding to H-mode plasmas) field line curvature plays a minor role. The turbulence is nonlinearly sustained even if curvature is removed and all modes are linearly stable due to magnetic shear. In the nonlinear regime without curvature the system obeys a different scaling law compared to the low $\alpha$ regime. The transport scaling is discussed in both regimes and the implications for OH-, L-mode and H-mode transport are discussed.

*Die nachstehende Arbeit wurde im Rahmen des Vertrages zwischen dem Max-Planck-Institut für Plasmaphysik und der Europäischen Atomgemeinschaft über die Zusammenarbeit auf dem Gebiete der Plasmaphysik durchgeführt.*

# 1 Introduction

The role of plasma turbulence as the main source of transport in toroidal confinement devices has stimulated a large amount of theoretical and experimental work. The particular importance of the plasma edge turbulence is demonstrated by the L-H transition where the formation of a transport barrier at the plasma edge leads to a dramatic improvement of the global confinement. Since the edge transport also determines the width of the scrape-off layer (SOL), knowledge of the transport scaling is required to estimate the divertor heat load of future tokamak experiments and to design the geometry of closed divertors.

We present the results of 3-D simulations of tokamak edge turbulence with realistic parameters in toroidal geometry. Our work is related to that presented in several previous publications (see Ref. [1] and citations). Due to the high collisionality at the plasma edge we use a two-fluid model. We include the field line curvature since measurements of fluctuations in the edge display an inside/outside asymmetry, the amplitudes being larger on the outside where the curvature is unfavourable [2][3]. Heat load measurements at the divertor plates also indicate that transport on the outside of the torus exceeds that on the inside, consistent with the curvature as a drive of the transport [4][5][6]. The structure of the turbulence is largely controlled by a single dimensionless parameter $\alpha$, the ratio of the ideal ballooning growth rate to the drift wave frequency, which governs the transition from resistive ballooning to drift wave turbulence. If this parameter is evaluated for experimentally observed plasma edge parameters, L-mode plasmas fall in the resistive ballooning regime and H-mode plasmas in the drift wave regime. The linear analysis of the unstable modes in the two fluid model was presented in Refs. [7][8] (and citations within). A set of nonlinear two-fluid equations were derived and used to simulate turbulence and transport in a flux tube system [1], but due to the numerical approach the simulations were restricted to the resistive ballooning regime with reduced magnetic shear and the time interval of the runs was quite short. Improvements of the numerical algorithms enable us to treat the whole parameter space and to correctly deal with the large parallel correlation length. Periodic boundaries in the radial direction ensure steady state conditions by avoiding profile flattening. Finally implicit time stepping allows us to run far into the nonlinear regime where fluctuations and transport evolve to quasi-steady levels.

In section 2 the basic equations are described and transformed to a dimensionless form which is adequate for the ballooning space and time scales and for the use in a flux tube coordinate system. In section 3 we present our numerical results including the observations related to a new nonlinear instability [9]. In section 4 the values of the dimensionless parameters are computed for realistic tokamak edge profiles of ASDEX and the implications of our results for understanding the edge turbulence in this machine are discussed. Our numerical methods are explained in the Appendix.

## 2 Equations and Computational Domain

Since the complete derivation of the equations is reported elsewhere [1], it is only summarized briefly here. The basic nonlinear equations are the reduced Braginskii equations [10]

$$\frac{dn}{dt} - 2n\vec{\kappa}\cdot\vec{v}_\perp^0 - \nabla\cdot\left(\frac{nc}{\Omega_i B}\frac{d}{dt}\nabla_\perp\phi\right) + \nabla_\parallel\left(nv_\parallel\right) = 0, \tag{1}$$

$$\nabla\cdot\left(\frac{nc}{\Omega_i B}\frac{d}{dt}\nabla_\perp\phi\right) - \frac{2cT_e}{eB}\vec{b}\times\vec{\kappa}\cdot\nabla n - \nabla_\parallel\frac{j_\parallel}{e} = 0, \tag{2}$$

$$\frac{dv_\parallel}{dt} = -\frac{c_s^2}{n}\nabla_\parallel n, \tag{3}$$

where $\vec{v}_\perp^0 = -c\nabla\phi\times\vec{b}/B$, $d/dt = \partial/\partial t + \vec{v}_\perp^0\cdot\nabla$ and $\eta j_\parallel = -\nabla_\parallel\phi + (T_e/e)\nabla_\parallel \ln n$ with $\eta$ the classical resistivity, $\vec{b} = \vec{B}/B$ the direction of the magnetic field and $\vec{\kappa} = \vec{b}\cdot\nabla\vec{b}$ the field line curvature.

The ions are assumed to be cold and the electron temperature is kept constant. The first term in the continuity equation (1) includes $E\times B$ convection, the second results from the divergence of the $E\times B$ flow, which is nonzero in a curved magnetic field, the third arises from the divergence of the ion polarization drift and the last term describes the divergence of the parallel flow. The vorticity equation (2) balances the currents from the two species insuring quasineutrality. The first and second terms are the charge flow due to the ion polarization drift and the electron curvature drift respectively. These perpendicular drifts are balanced by parallel currents which are connected to the density and the potential by Ohm's law. Finally the velocity equation (3) describes the sound wave propagation along the magnetic field due to parallel density gradients. In the toroidal coordinate system the operators take the form

$$\nabla_\parallel = \frac{1}{R}\left(\frac{\partial}{\partial\varphi} + \frac{1}{q}\frac{\partial}{\partial\theta}\right), \tag{4}$$

$$\vec{b}\times\vec{\kappa}\cdot\nabla = -\frac{1}{R}\left(\frac{\cos\theta - \epsilon}{a}\frac{\partial}{\partial\theta} + \sin\theta\frac{\partial}{\partial r}\right). \tag{5}$$

Because of high parallel conductivity, disturbances of $\phi$ and $n$ have large parallel correlation lengths along $\vec{B}$. To minimize the size of the computational domain required to describe such fluctuations, we transform the equations to a field line coordinate system [11] in which $z$ lies along the local $\vec{B}$ and $x$, $y$ are transverse to $\vec{B}$. The transformation is defined by

$$x = r,\ y = a\left[\theta - (\varphi - \varphi_0)/q\right] - a\varphi_0/q_a,\ z = R\varphi. \tag{6}$$

In this coordinate system the operators are given by

$$\nabla_\parallel = \frac{\partial}{\partial z}, \tag{7}$$

$$\vec{b} \times \vec{\kappa} \cdot \nabla =$$

$$-\frac{1}{R}\left\{[\cos(2\pi z/L_z) + 2\pi\hat{s}(z-z_0)/L_z \sin(2\pi z/L_z) - \epsilon]\frac{\partial}{\partial y} + \sin(2\pi z/L_z)\frac{\partial}{\partial x}\right\}, \quad (8)$$

$$\nabla f \times \vec{e}_\varphi \cdot \nabla = \frac{\partial f}{\partial y}\frac{\partial}{\partial x} - \frac{\partial f}{\partial x}\frac{\partial}{\partial y}, \quad (9)$$

$$\nabla_\perp^2 = \left\{\frac{\partial}{\partial x} + [2\pi\hat{s}(z-z_0)/L_z]\frac{\partial}{\partial y}\right\}^2 + \frac{\partial^2}{\partial y^2}, \quad (10)$$

where we have used the abbreviations $\hat{s} = (a/q)\, dq/dr$, $L_z = 2\pi q_a R$, and $z_0 = R\varphi_0$. This coordinate system has the added advantage that there is no explicit $x$ dependence so that radial correlation lengths are a consequence of the nonlinearities in the system and not the variable resolution of the numerical grid. Since for diagnostic purposes we often use a helical flux tube system with a more 'natural' field line geometry we also write here the transformation to this system:

$$x' = x,\ y' = y - 2\pi\hat{s}(x - x_a)(z - z_0)/L_z,\ z' = z. \quad (11)$$

In this coordinate system the magnetic field is parallel to the $z$-direction only at the radial plane $x = x_a$; at different locations it is inclined according to the magnetic shear $\hat{s}$.

Characteristic space and time scales are obtained [1] by using the ballooning property of the equations. If the perpendicular wave-length is small, the parallel gradient term in the vorticity equation (2) is negligible, leading to the ideal ballooning growth rate $\gamma_0 = c_s/(L_n R)^{1/2}$, with $c_s = (T_e/m_i)^{1/2}$ and $L_n = -n/(dn/dx)$ the density e-folding length. Balancing the involved terms leads to the characteristic time scale

$$t_0 = \left(\frac{RL_n}{2}\right)^{1/2}\frac{1}{c_s}. \quad (12)$$

Taking $\nabla_\parallel \sim L_z^{-1}$ the perpendicular scale length $L_0$ is obtained by balancing the first and the third term in (2):

$$L_0 = 2\pi q_a \left(\frac{\nu_{ei} R\rho_s}{2\Omega_e}\right)^{1/2}\left(\frac{2R}{L_n}\right)^{1/4} = 2\pi q_a \left(\frac{ne^2\eta_\parallel \rho_s R}{m_e\Omega_e}\right)^{1/2}\left(\frac{2R}{L_n}\right)^{1/4}. \quad (13)$$

Inserting these scalings into the equations, we obtain immediately the scaling for the density fluctuation, the potential and the parallel velocity:

$$\tilde{n} \sim n_0\frac{L_0}{L_n}, \quad \phi \sim \frac{B}{c}\frac{L_0^2}{t_0}, \quad v_\parallel \sim c_s\frac{L_0}{L_n}, \quad (14)$$

with $n_0$ denoting the background density and $\tilde{n} = n - n_0$ the density fluctuation. This leads to the dimensionless equations in field aligned coordinates:

$$\frac{d}{dt}\nabla_\perp^2\phi + \hat{C}n + \frac{\partial^2 h}{\partial z^2} = D_\phi\nabla_\perp^4\phi, \quad (15)$$

$$\frac{dn}{dt} + \frac{\partial \phi}{\partial y} - \epsilon_n \hat{C} h + \epsilon_n \alpha \frac{\partial^2 h}{\partial z^2} + \gamma \frac{\partial}{\partial z} v_{\|} = D_n \nabla_\perp^2 n, \tag{16}$$

$$\frac{dv_{\|}}{dt} = -\gamma \frac{\partial n}{\partial z}, \tag{17}$$

with

$$\hat{C} = [\cos(2\pi z) + 2\pi \hat{s}(z - z_0)\sin(2\pi z) - \epsilon]\frac{\partial}{\partial y} + \sin(2\pi z)\frac{\partial}{\partial x},$$

$$\nabla_\perp^2 = \left[\frac{\partial}{\partial x} + 2\pi \hat{s}(z - z_0)\frac{\partial}{\partial y}\right]^2 + \frac{\partial^2}{\partial y^2},$$

$$\frac{d}{dt} = \frac{\partial}{\partial t} - \nabla_\perp \phi \times \vec{e}_z \cdot \nabla_\perp = \frac{\partial}{\partial t} - \left(\frac{\partial \phi}{\partial y}\frac{\partial}{\partial x} - \frac{\partial \phi}{\partial x}\frac{\partial}{\partial y}\right)$$

$$h = \phi - \alpha n, \quad \alpha = \frac{\rho_s c_s t_0}{L_n L_0}, \quad \gamma = \frac{c_s t_0}{L_z}, \quad \epsilon_n = \frac{2L_n}{R}, \quad \hat{s} = \frac{a}{q_a}\frac{\partial q_a}{\partial r},$$

and the additional viscosities $D_n$ and $D_\phi$. Compared to the well-known Hasegawa-Wakatani equations [12] we obtain additional terms due to field line curvature, which are all contained in the operator $\hat{C}$, and an additional equation describes the parallel flow. The anomalous particle transport coefficient is related to the particle flux from the simulations through

$$D_{an} = D_0 \langle n v_{radial} \rangle = -D_0 \langle n \frac{\partial \phi}{\partial y} \rangle \tag{18}$$

with the intrinsic transport given by

$$D_0 = (2\pi q_a)^2 \rho_e^2 \nu_{ei} \frac{R}{L_n}. \tag{19}$$

Since we evaluate the flux as a function of the parallel coordinate the brackets $\langle\ \rangle$ denote an average over the poloidal plane $x$ and $y$.

Multiplying Eqs. (15), (16) and (17) by $n$, $\phi$ and $v_{\|}$ respectively, integrating over all space and combining the resulting equations, we obtain the total rate of change of energy

$$\frac{1}{2}\frac{d}{dt}\int \left[(\nabla_\perp \phi)^2 + \frac{1}{\epsilon_n}(n^2 + v_{\|}^2)\right] d^3x =$$

$$-\int \left[\frac{n}{\epsilon_n}\frac{\partial \phi}{\partial y} + \left(\frac{\partial h}{\partial z}\right)^2 + D_\phi \left(\nabla_\perp^2 \phi\right)^2 + \frac{D_n}{\epsilon_n}(\nabla_\perp n)^2\right] d^3x. \tag{20}$$

The terms on the left hand side correspond to perpendicular kinetic energy, internal energy and parallel kinetic energy respectively. On the right hand side only the first term can act as a source. It describes the extraction of energy from the density profile. The damping terms appear as sinks since the temperature equations have been discarded. In our numerical simulations this energy theorem is used to monitor the accuracy of the time stepping algorithm.

Stabilization of edge turbulence by sheared poloidal rotation has been proposed as a mechanism for turbulence suppression at the L-H transition. Two distinct mechanisms follow from a fluid treatment of edge turbulence: Reynolds stress [13][14] and Stringer spin-up [15][16][17][18]. The Reynolds stress is produced by a self-induced distortion of fluid vortices and has been identified as a mechanism for sheared flow generation in a variety of simulations of plasma transport [1] [19]. Recent simulations of the Hasegawa-Wakatani equations in 3D [20] showed a very strong shear flow generation due to Reynolds stress. Since these simulations were performed without magnetic shear the behaviour of the present system may be different. The Stringer spin-up is a toroidal effect and is therefore not present in simple slab treatments of turbulence. It is related to a transport asymmetry between inside and outside of the torus which leads to parallel flows from the outside to the inside. To drive these parallel flows a radial pile-up of plasma pressure on the outside of the torus is required. Such effects cannot be included in a local transport model (in particular with periodic boundary conditions), hence the Stringer spin-up is not included in the present simulations.

# 3 Simulation Results

## 3.1 Simulation Results: $\alpha < 1$

Since the parameter $\alpha$ divides the turbulence into two different regimes, we separate the discussion of our simulations into low and high values of $\alpha$. Our low-$\alpha$ reference run was performed with the following parameters: $\alpha = 0.5$, $\epsilon_n = 0.04$, $\epsilon = 0.25$, $\gamma = 0.02$, $\hat{s} = 1.0$, $D^\phi = D^n = 0.002$. The box dimensions are $L_x = 5.73$, $L_y = 6$ transverse to $\vec{B}$, and $L_z = 3$ along $\vec{B}$, corresponding to three full periods of good and bad curvature. The poloidal plane is resolved by $64 \times 64$ complex modes in $x$ and $y$ direction and in $z$ direction we use 96 grid points. Starting from low-amplitude random noise the ballooning instability grows and forms extended streams in the radial direction at the unfavourable curvature location (see Fig. 1 at $z = 1.0$). The perturbation spreads along the magnetic field into the favourable curvature region. With increasing distance from the bad curvature region the extended streams become more and more inclined with respect to the radial direction due to the magnetic shear (Fig. 1 at $z = 0.75, 1.25$). In the favourable curvature region the perturbations due to the two neighbouring unfavourable curvature regions form a pattern of intersecting lines (Fig. 1 at $z = 0.5$). The ballooning character of the fluctuations is shown in Fig. 2 in this linear phase. The bad curvature regions are centered at $z = 0.0, \pm 1.0$. We obtain a pronounced peaking of the transport at the outside of the torus (Fig. 3). This strong peaking occurs because of the ballooning of the disturbances and because of the inclination of the flows on the torus inside compared with the torus outside. On the outside positive radial flows carry positive density perturbations outward, producing large transport. On the inside the magnetic shear causes the flows to tip in the poloidal direction, resulting

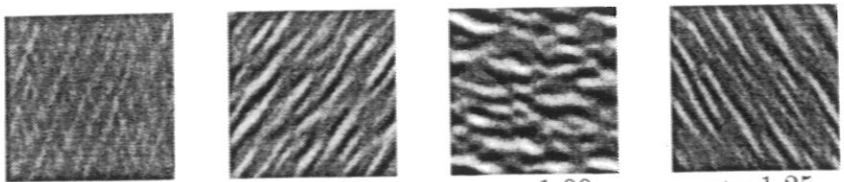


Figure 1: Structure of $n$ for $\alpha = 0.5$ in the linear regime. The plots show poloidal cross sections (transformed into the helical flux tube system) at different parallel locations. White corresponds to high density and black to low density. $z = 0.5$ corresponds to the favourable curvature location and $z = 1$ to the unfavourable curvature location. The density gradient points to the left and the poloidal angle increases upward.

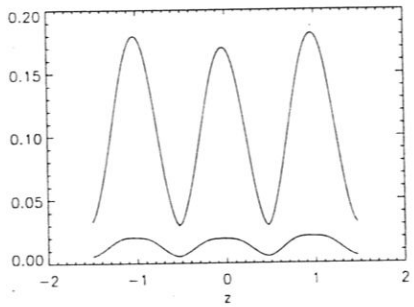


Figure 2: $\langle n^2 \rangle^{1/2}$ (upper line) and $\langle \phi^2 \rangle^{1/2}$ (lower line) during linear phase for $\alpha = 0.5$

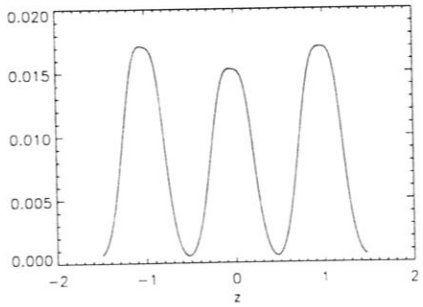


Figure 3: Radial transport during linear phase for $\alpha = 0.5$

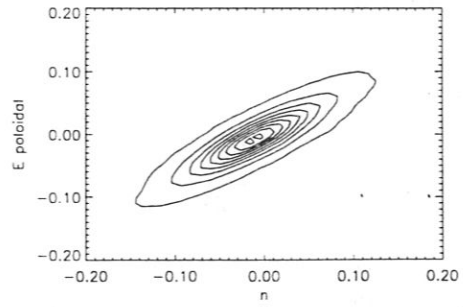


Figure 4: Probability distribution of density and poloidal electric field during linear phase for $\alpha = 0.5$

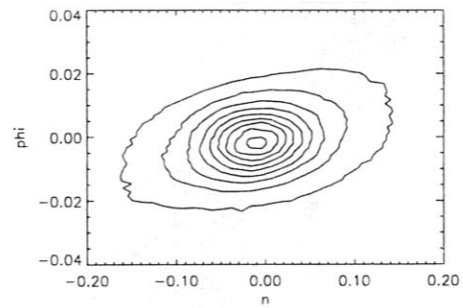


Figure 5: Probability distribution of density and potential during linear phase for $\alpha = 0.5$

in a lower transport level. The efficiency of the flows in driving transport can be seen from the probability distribution of $n$ and the poloidal electric field $E_{poloidal} \sim v_{rad}$ in Fig. 4. The strong alignment along the diagonal implies that the flows are very efficient in driving transport in the linear phase. Finally Fig. 5 shows that there is no correlation between density and potential.

When the streams become sufficiently strong entering the nonlinear phase they break up because of the Kelvin-Helmholtz instability. They form mushroom-like density blobs with high density streaming outward and low density inward (Fig. 6). In the parallel direction the variation is weak leading only to a twist of the pattern along the magnetic field which can still be seen in Fig. 6. This behaviour is confirmed by the autocorrelation function of $n$, $\phi$ and $h$ in parallel direction (Fig. 7). On the other hand the parallel correlation length is sufficiently short to decorrelate the turbulence within the chosen length of the flux tube, hence justifying the pseudo-periodic boundaries in parallel direction (the numerical approach is described in detail in the Appendix). In addition the correlation length is too short to invoke

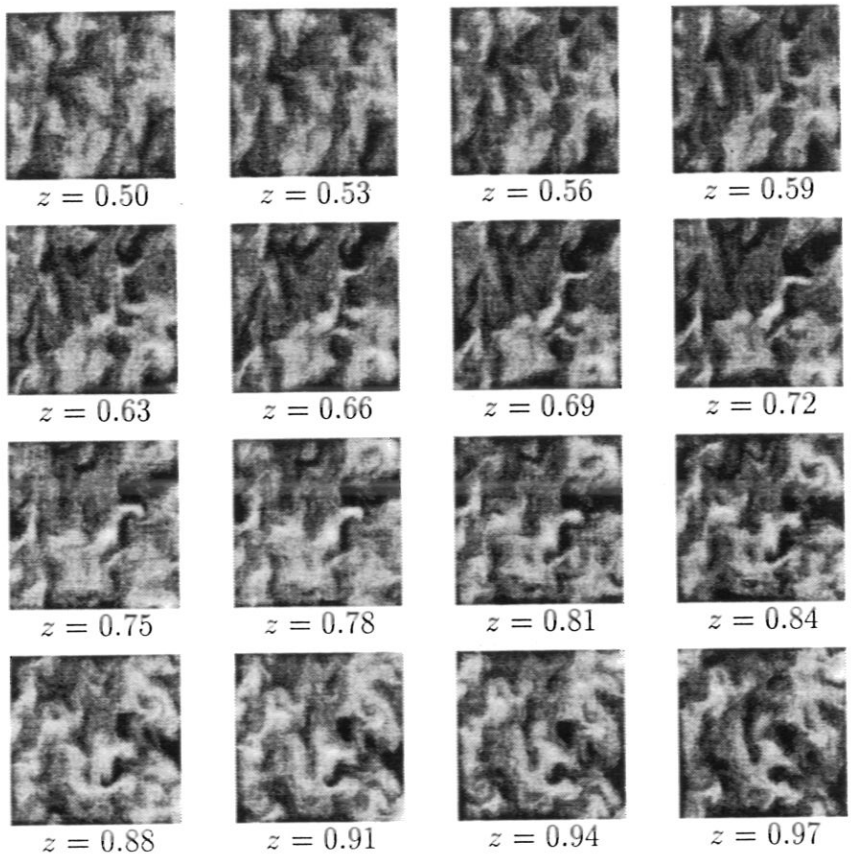


Figure 6: Structure of $n$ for $\alpha = 0.5$ at different locations along the magnetic field. The plots show poloidal cross sections (transformed into the helical flux tube system) at saturation, beginning in the favourable curvature region and ending in the unfavourable curvature region.

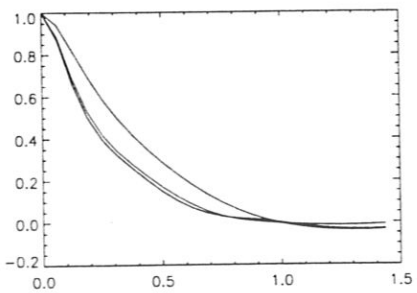


Figure 7: Autocorrelation function in parallel direction of $n$, $\phi$ (lower lines) and $h$ (upper line) for $\alpha = 0.5$

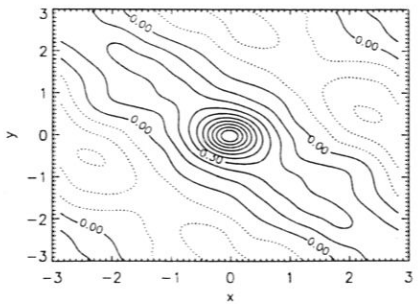


Figure 8: Correlation of the density $\langle n(x_0+x, y_0+y)n(x_0,y_0)\rangle_{x_0,y_0}$ at the outside midplane for $\alpha = 0.5$

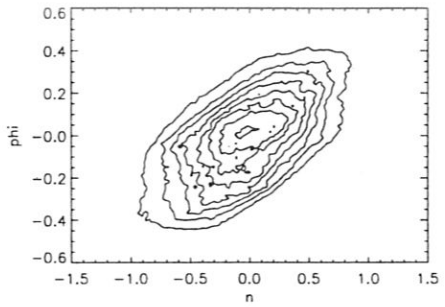


Figure 9: Probability distribution of density and potential in a saturated state for $\alpha = 0.5$

any rational surface effects in experimental geometry. The stationary turbulence is nearly isotropic in the poloidal plane. This can be seen clearly in the corresponding correlation function of $n$ shown in Fig. 8. Note, however, that the correlation function has a weak tail which fluctuates around the radial direction. This reflects the tendency of the disturbances to stream radially due to the unfavourable curvature. Compared to the linear phase (Fig. 5), there is now a definite correlation between $\phi$ and $n$ (Fig. 9). The width of the distribution function on the other hand shows that the nonadiabatic contribution is still significant. To measure the relation between $\phi$ and $n$ we define the adiabaticity parameter

$$\delta = \frac{\langle(\phi - \alpha n)^2\rangle}{\langle\phi^2 + \alpha^2 n^2\rangle} \tag{21}$$

with the brackets $\langle\ \rangle$ denoting the average over the whole domain. $\delta$ is one when $\phi$ and $n$ are completely uncorrelated and zero if the system is adiabatic. For the state shown in Fig. 9 we obtain $\delta = 0.37$. Short scale structures (compared to the linear phase) are present only in the density whereas the potential remains smooth. The

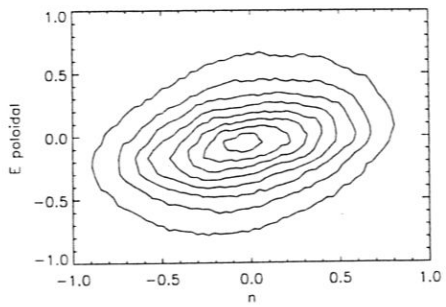


Figure 10: Probability distribution of density and poloidal electric field in a saturated state for $\alpha = 0.5$

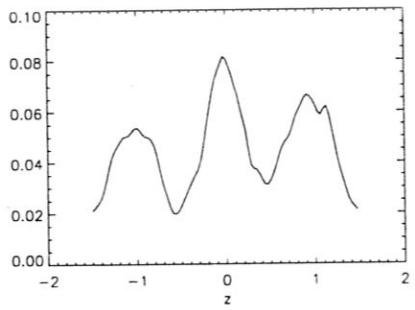


Figure 11: Radial flux $\langle nv_{rad} \rangle$ in a saturated state for $\alpha = 0.5$

increased correlation between $n$ and $\phi$ leads to a reduction of the correlation between $n$ and the radial velocity (Fig. 10). Nevertheless low density is still correlated to an inward velocity and high density to an outward velocity leading to anomalous transport (Fig. 11). Finally the mean square fluctuation levels of $n$ and $\phi$ retain the ballooning property also in the saturated turbulent state (Fig. 12). Since the turbulence is now more adiabatic, the potential is more closely connected to the density, leading to a relatively stronger fluctuation amplitude of $\phi$.

A series of simulations have been performed in the regime of $\alpha < 1$. The most pronounced ballooning behaviour is obtained for $\alpha = 0$. For this run the dependence of the transport on $z$ in the nonlinear saturated regime remains smooth similar to the linear phase in Fig. 3 in contrast to the more noisy and fluctuating behaviour for $\alpha = 0.5$ (Fig. 11). The diamagnetic propagation is weak for $\alpha < 1$ decreasing with decreased $\alpha$. The correlation between $n$ and $\phi$ becomes significantly stronger with increased $\alpha$. Since the correlation is produced by the parallel diffusion of the nonadiabatic contribution $h = \phi - \alpha n$, for $\alpha = 0$ there is no correlation between $\phi$ and $n$ and the adiabaticity parameter $\delta$ is unity.

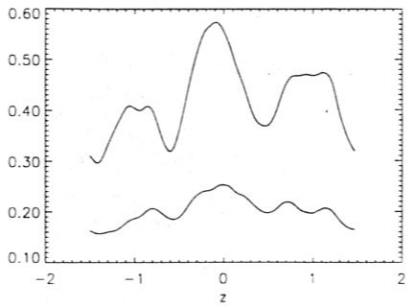


Figure 12: $\langle n^2 \rangle^{1/2}$ (upper line) and $\langle \phi^2 \rangle^{1/2}$ (lower line) in a saturated state for $\alpha = 0.5$

As discussed in section 1 Reynolds stress as a mechanism for shear-flow generation is included. Nevertheless we do not observe a significant stationary shear flow for $\alpha \geq 0.5$ (also in the regime $\alpha > 1$ dicussed in the next section). Only a simulation with $\alpha = 0$ led to a stationary shear-flow which was sufficient to reduce the level of turbulence significantly.

A surprising result of the simulations is that the level of the transport in the range $0.5 \leq \alpha \leq 1$ is insensitive to $\alpha$. In the unfavourable curvature region $\langle n v_{rad} \rangle$ is approximately $0.070 \pm 0.015$ and in the favourable curvature region $0.035 \pm 0.010$. According to linear theory, increasing $\alpha$ leads to diamagnetic stabilization of the long wavelength modes and a shift of the spectrum to short wavelength. Thus, we expected that larger $\alpha$ would correlate with reduced transport. The reason why this does not happen will be discussed in the next section.

## 3.2 Simulation Results: $\alpha > 1$

In the high-$\alpha$ regime the system is still linearly unstable if $\alpha$ is less than approximately 1.5. Above this value long-wavelength resistive ballooning modes are stabilized by the large electron diamagnetic drift and short wavelength modes are stabilized by viscosity (which is at a realistic level for the tokamak edge). The usual slab drift-wave is stabilized by magnetic shear [21]. For reference we discuss two simulations with $\alpha = 1.25$ and $\alpha = 1.5$ and all other parameters as in the $\alpha = 0.5$ run discussed earlier. The size of the computational box in the transverse plane is varied to ensure that the structure of the turbulence does not depend on the periodicity assumptions. In both runs in the linear phase ballooning modes grow as at low $\alpha$ but with significantly reduced growth rates and at shorter wavelength. As the turbulence saturates it undergoes a qualitative change in structure: the fluctuations

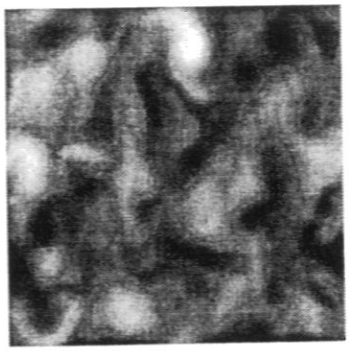

Figure 13: Poloidal cross section of $n$ for $\alpha = 1.5$

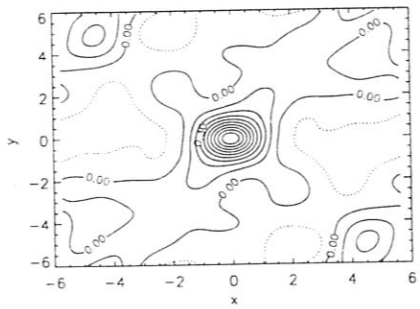


Figure 14: Correlation of the density at the outside midplane for $\alpha = 1.5$

evolve to much longer wavelength and form structures which clearly propagate at the electron diamagnetic velocity (as the linear modes do). A plot of the density perturbation in the bad curvature region at late time from the $\alpha = 1.5$ run is shown in Fig. 13. The mushroom-like structures which were evident at low $\alpha$ are absent, the fluctuations are much smoother, and the scale lengths are larger. Note that in Fig. 13 the computational box is doubled compared with the $\alpha = 0.5$ case in Fig. 6. The increased scale length of the turbulence is reflected in a broadening of the transverse correlation function of the density for $\alpha = 1.5$ shown in Fig. 14 compared with the corresponding plot for $\alpha = 0.5$ (Fig. 8, note the different scale). For this high $\alpha$ case the tail on the correlation function corresponding to radial streaming is absent. The corresponding autocorrelation functions of $h$, $\phi$ and $n$ in the $z$ direction are shown in Fig. 15. The function $h$ has a modestly larger field-aligned correlation than for $\alpha = 0.5$ but it remains shorter than the parallel length of our computational box. The drift-wave-like propagation is a consequence of the increased adiabaticity of the fluctuations as measured by the parameter $\delta$, which is now 0.21 compared to 0.37 with $\alpha = 0.5$. Figure 16 shows the mean-squared values of $n$ and $\phi$ as a

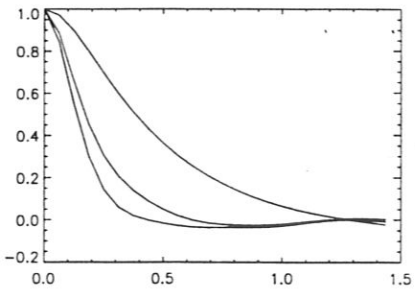


Figure 15: Autocorrelation function in parallel direction of $h$ (upper line), $n$ (middle line) and $\phi$ (lowest line) for $\alpha = 1.25$

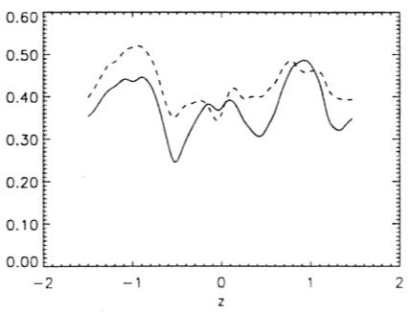


Figure 16: $\langle n^2 \rangle^{1/2}$ (solid line) and $\langle \phi^2 \rangle^{1/2}$ (dashed line) in a saturated state for $\alpha = 1.25$

function of $z$. The larger value of $\phi$ compared to $\alpha = 0.5$ is due to the increased adiabaticity which requires $\phi \simeq \alpha n$ and therefore larger $\phi$ fluctuations as $\alpha$ is increased. The transport level is $0.075 \pm 0.010$ at the unfavourable curvature location and $0.040 \pm 0.005$ at the favourable curvature location which is almost exactly the same level as in the low $\alpha$ case in spite of the significantly reduced linear growth rate of the instability in the high $\alpha$ regime.

The unexpected change of the character of the turbulence after saturation and the surprisingly high level of transport given the weakness of the linear instability in comparison with the case $\alpha = 0.5$ suggest the existence of an additional (nonlinear) drive mechanism. Nonlinear instabilities in drift wave turbulence have previously been discussed [22][23]. To test this hypothesis we removed the curvature drive (all terms containing the operator $\hat{C}$) in our equations and restarted a run for $\alpha = 1.25$ from a saturated state at late time. Even without curvature the transport remained at almost the same level although the system was linearly stable. By contrast the turbulence in the $\alpha = 0.5$ run immediately died away when we removed the curvature. As expected, without curvature the mean properties of the turbulence became homogeneous in $z$ direction. At the former bad curvature location the transport level modestly decreased and at the favourable curvature location increased. To further check that our boundary conditions do not introduce a spurious instability in this sheared slab system, we completed a run at $\alpha = 1.25$ from noise with the curvature removed. The fluctuations died away as expected. We have recently shown that the source of the nonlinear instability is the self-consistent nonlinear amplification of radial flows [9]. This nonlinear mechanism completely dominates the usual linear drift-wave drive even in the absence of magnetic shear.

The turbulence and transport which develops from the reduced set of equations without the curvature drive obeys a different scaling than with curvature. We derive the new scaling laws by dropping all curvature terms and, for simplicity, terms containing the parallel velocity in Eqs. (15), (16) and by rescaling the system according to $\tilde{x} = x/L_\perp$, $\tilde{y} = y/L_\perp$, $\tilde{z} = z\hat{s}$, $\tilde{t} = t\alpha/L_\perp$, $\tilde{\phi} = \phi/\alpha L_\perp$, $\tilde{n} = n/L_\perp$ with $L_\perp = \alpha^{1/3}/\hat{s}^{2/3}$. We obtain equations similar to the Hasegawa-Wakatani system with magnetic shear

$$\frac{d}{dt}\nabla_\perp^2 \phi = -\frac{\partial^2}{\partial z^2}(\phi - n) \tag{22}$$

$$\frac{dn}{dt} + \frac{\partial \phi}{\partial y} = -\hat{\rho}^2 \frac{\partial^2}{\partial z^2}(\phi - n) \tag{23}$$

with $\nabla_\perp^2 = (\partial/\partial x + 2\pi z \partial/\partial y)^2 + \partial^2/\partial y^2$, where the tilde has been dropped, and $\hat{\rho}^2 = \epsilon_n(\alpha\hat{s})^{4/3}$. The transport in the new variables is given by

$$D_{an} = \hat{D}_0 \langle n \frac{\partial \phi}{\partial y} \rangle, \qquad \hat{D}_0 = D_0 \frac{\alpha^{4/3}}{\hat{s}^{2/3}}.$$

The governing parameter now is $\hat{\rho}^2 = \epsilon_n(\alpha\hat{s})^{4/3}$. To explore the variation of the transport with this parameter, we completed a series of simulations without curvature with different values of $\epsilon_n$ while keeping $\alpha = 1.25$ and $\hat{s} = 1$. The fluctuation

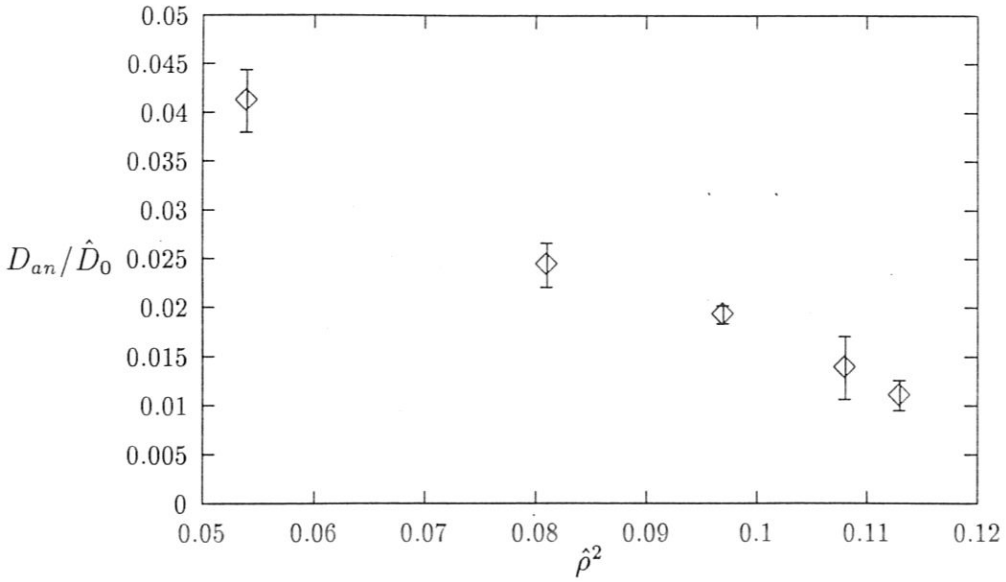


Figure 17: Transport versus $\hat{\rho}^2$. The errorbars represent the standard deviation due to the time variation of the flux.

amplitudes monotonically decreased with increasing $\epsilon_n$ although the characteristic scale lengths and drift-wave-like propagation properties remained unchanged. The variation of the average flux with $\hat{\rho}^2$ is shown in Fig. 17. Above $\hat{\rho}^2 = 0.15$, the nonlinear drive mechanism becomes extremely weak and the development of sheared flow triggers the collapse of the nonlinear instability and subsequent decay to zero amplitude.

# 4 Comparison with ASDEX Results

Having identified the key parameters which control the drive mechanisms and structure of tokamak edge turbulence, we now discuss the implications of the results for understanding edge turbulence in real machines. At the present time this discussion must remain qualitative since key ingredients such as the coupling between a SOL, with appropriate boundary conditions at the divertor or limiter plates, and the closed flux region are not properly treated in the present model. Our discussion focuses on data from the ASDEX experiment although the qualitative conclusions also apply to DIII-D. The experimental values of the dimensionless parameters are calculated from edge data [24]. Since for this purpose the cold-ion approximation is not appropriate ($T_i > T_e$ in L-mode and H-mode), we modify our equations to include $T_i = const. \neq 0$. The inclusion of the ion diamagnetic drift in the ion continuity equation leads to an additional term $-2n\vec{\kappa} \cdot \vec{v}_{di}$ arising from $\nabla \cdot n\vec{v}_{di}$ with $\vec{v}_{di} = (cT_i/enB)\vec{b} \times \nabla n$ the ion diamagnetic velocity. In the vorticity equation the

| | OH | OH | L | L | L | L | H | H | H |
|---|---|---|---|---|---|---|---|---|---|
| $r[cm]$ | 0 | -1 | 0.7 | 0 | -1 | -2 | 0.2 | 0 | -1 |
| $R[cm]$ | 165 | 165 | 165 | 165 | 165 | 165 | 165 | 165 | 165 |
| $B[T]$ | 2.2 | 2.2 | 2.2 | 2.2 | 2.2 | 2.2 | 2.2 | 2.2 | 2.2 |
| $Z_{eff}$ | 2 | 2 | 4 | 4 | 4 | 4 | 4 | 4 | 4 |
| $q_a$ | 3.5 | 3.5 | 3.5 | 3.5 | 3.5 | 3.5 | 3.5 | 3.5 | 3.5 |
| $m_i/m_p$ | 2 | 2 | 2 | 2 | 2 | 2 | 2 | 2 | 2 |
| $T_e[eV]$ | 70 | 110 | 70 | 130 | 170 | 210 | 150 | 240 | 325 |
| $\tau$ | 0.5 | 0.5 | 1 | 1 | 1 | 1 | 1 | 1 | 1 |
| $n[10^{13}cm^{-3}]$ | 0.8 | 1.1 | 0.4 | 0.6 | 0.82 | 1.0 | 0.4 | 0.6 | 1.2 |
| $n'[10^{12}cm^{-4}]$ | 3.3 | 2.5 | 3.0 | 2.4 | 2.0 | 1.3 | 4.8 | 6.0 | 5.5 |
| $L_n[cm]$ | 2.4 | 4.4 | 1.33 | 2.5 | 4.16 | 7.5 | 0.83 | 1.0 | 2.2 |
| $t_0[10^{-6}s]$ | 2.0 | 2.14 | 1.28 | 1.29 | 1.45 | 1.76 | 0.69 | 0.6 | 0.76 |
| $L_0[cm]$ | 0.29 | 0.24 | 0.37 | 0.29 | 0.26 | 0.23 | 0.3 | 0.28 | 0.27 |
| $\alpha$ | 0.9 | 1.0 | 0.82 | 1.0 | 1.0 | 1.0 | 1.9 | 2.37 | 1.86 |
| $\epsilon_n$ | .029 | .053 | .016 | .03 | .05 | .091 | .01 | .012 | .027 |
| $\gamma$ | .004 | .005 | .003 | .004 | .005 | .007 | .002 | .003 | .004 |
| $\epsilon_n\alpha^{4/3}(1+\tau)$ | .04 | .08 | .02 | .06 | .1 | .18 | .05 | .08 | .12 |
| $D_0[10^5cm^2/s]$ | 0.43 | 0.27 | 1.1 | 0.66 | 0.48 | 0.29 | 1.3 | 1.3 | 1.0 |
| $D_{num}[m^2/s]$ | 0.25/0.12 | | 0.5/0.25 | | | | 1.2 | 1.0 | 0.2 |

Table 1: Edge data of ASDEX (OH, L-mode, H-mode). The last line shows a rough estimate of the anomalous diffusion rate based on our simulations. The two values under Ohmic and L-mode conditions correspond to the regions of unfavourable and favourable curvature.

total pressure appears in the curvature drive so that $T_e$ is replaced by $T_e + T_i$. The nonlinearity due to the diamagnetic contribution to the $\nabla_\perp\phi$ convection (see Ref. [8]) appears in the vorticity equation. The altered equations are given by

$$\frac{d}{dt}\nabla_\perp^2\phi - \alpha\tau\nabla_\perp\cdot[(\vec{e}_y - \vec{e}_z\times\nabla n)\cdot\nabla]\nabla_\perp\phi + \hat{C}n + \nabla_\parallel^2 h = 0,$$

$$\frac{dn}{dt} + \frac{\partial\phi}{\partial y} - \epsilon_n\hat{C}h + \epsilon_n\alpha(1+\tau)\nabla_\parallel^2 h + \gamma\nabla_\parallel v_\parallel = 0,$$

$$\frac{dv_\parallel}{dt} = -\gamma\frac{\partial n}{\partial z},$$

with $c_s = (T_e(1+\tau)/m_i)^{1/2}$, $\tau = T_i/T_e$, $\alpha = (\rho_s c_s t_0)/(L_n L_0(1+\tau))$ and all other quantities as defined previously (the viscous terms have been dropped). The only change in the equations is the factor $1+\tau$ in the continuity equation and the diamagnetic drift in the vorticity equation.

Table 1 shows the parameters for L-mode, H-mode and Ohmic plasmas of ASDEX [24]. We emphasize that the uncertainties in the parameters are substantial

(especially $Z_{eff}$, $\tau$ and $L_n$) so that only qualitative trends should be taken seriously. Both Ohmic and L-mode plasmas correspond to $\alpha \sim 1$. According to our simulations (see section 3) the transport is dominantly driven by the ballooning instability in this $\alpha$ regime. The transport increases in L-mode compared to Ohmic because of increased $Z_{eff}$ and $\tau$. For the ASDEX H-mode $\alpha \sim 2$ and our system is linearly stable. Nevertheless the turbulence is sustained by a nonlinear instability (section 3.2). In this high-$\alpha$ regime the crucial parameter is $\hat{\rho}^2 = \epsilon_n(\alpha\hat{s})^{4/3}(1+\tau)$ and the transport decreases rapidly as this parameter is increased. At the separatrix and in the SOL in H-mode the transport from the nonlinear instability for $\hat{\rho}^2 = 0.5 - 0.8$ remains high while at 1 cm inside where $\hat{\rho}^2 = 0.12$ it is drastically reduced. This behaviour suggests the following scenario: transport in L-mode and Ohmic plasmas is driven by the resistive ballooning instability; a rise of the edge temperature increases $\alpha$ until it enters the regime where the ballooning drive becomes weak. At this stage the level of turbulence and transport depends strongly on $\hat{\rho}^2$. Near the separatrix transport is self-sustained while at the larger values of $\hat{\rho}^2$ interior to the separatrix the fluctuations are suppressed and a transport barrier develops. Whether this transport barrier then propagates radially outward and suppresses turbulence in the SOL can not be addressed in our present model.

# 5 Conclusions

The drift resistive ballooning equations produce two distinctly different types of turbulence, resistive ballooning and drift-wave, depending on the value of the diamagnetic parameter $\alpha$, which is the ratio between drift wave frequency and the linear ballooning growth rate. The structure of the turbulence as well as the intrinsic scaling of the transport differs in the two regimes. The ballooning regime is characterized by a large asymmetry of turbulence and transport between the high and low field sides of the torus and relatively weak diamagnetic propagation. At high values of $\alpha$ the diamagnetic drifts and perpendicular viscosity combine to stabilize all linear modes of the system. Nevertheless, the turbulence remains strong as a consequence of a nonlinear drive mechanism [9]. In this regime the turbulence has a relatively weak ballooning character, propagates in the electron diamagnetic direction and has a larger transverse correlation length. The scaling of the transport in the high $\alpha$, drift-wave regime is controlled by a parameter $\hat{\rho} = \rho_s/L_\perp$, where $\rho_s$ is the ion Larmor radius based on $T_e$ and $L_\perp$ is the transverse scale length of the drift-wave turbulence. The transport driven by the nonlinear instability decreases rapidly with increasing $\hat{\rho}$ up to a critical value, above which the turbulence completely dies away.

A comparison with experimental edge profiles suggests that OH- and L-mode are characterized by $\alpha \sim 1$ ballooning turbulence with L-mode transport exceeding that in Ohmic plasmas as a result of increased impurity content and increased ion temperature. H-mode falls in the high $\alpha$ regime where all linear modes are stabilized. At the separatrix and in the SOL the parameters are such that the nonlinear instability

can self-sustain turbulence while interior to the separatrix collapse of the turbulence should occur. A complete understanding of the L-H transition will require a proper treatment of the interface between the SOL and closed flux region.

## Acknowledgements

J. F. D. acknowledges the support of the Humboldt Foundation through a Senior Scientist Research Award at IPP-Garching. We like to thank Dr. Bruce Scott for significant discussion on the nature of drift wave turbulence. We also would like to thank Dr. E. Holzhauer and Dr. H. Niedermeyer for useful discussions about the experimental observations on ASDEX and W7-AS.

## References

[1] P. N. Guzdar, J. F,. Drake, D. C. McCarthy, A. B. Hassam, and C. S. Liu, Phys. Fluids B **5**, 3712 (1993).

[2] R. J. Taylor, M. L. Brown, B. D. Fried, H. Grote, J. R. Liberati, G. J. Morales, P. Pribyl, D. Darrow, and M. Ono, Phys. Rev. Lett. **63**, 2365 (1989).

[3] G. Tynan, "On the origin of tokamak edge turbulence and the H-mode transition", (to be published, 1995).

[4] B. LaBombard and B. Lipschultz, Nucl. Fusion **27**, 81 (1987).

[5] V. A. Vershkov and the T-10 and the CIEP Group, J. Nucl. Mat. **162-164**, 195 (1989); R. A. Pitts, G. Vayakis, G. F. Matthews, and V. A. Virshkov, J. Nucl. Mat. **176-177**, 893 (1990).

[6] D. Post and the ITER Divertor Modeling Team, in **Plasma Physics and Contr. Nucl. Fusion Res.** (IAEA, Vienna, 1994).

[7] D. McCarthy, P. N. Guzdar, J. F. Drake, T. M. Antonsen, Jr., and A. B. Hassam, Phys. Fluids B **4**, 1846 (1992).

[8] S. V. Novakovskii, P. N. Guzdar, J. F. Drake, C. S. Liu, Phys. Plasmas **2**, 781 (1995).

[9] J. F. Drake, A. Zeiler, and D. Biskamp, submitted.

[10] J. F. Drake and T. M. Antonsen, Jr., Phys. Fluids **27**, 898 (1984).

[11] A. M. Dimits, Phys. Rev. E **48**, 4070 (1993); M. A. Beer, S. C. Cowley, and G. W. Hammett, Phys. Plasmas **2**, 2687 (1995).

[12] A. Hasegawa and M. Wakatani, Phys. Rev. Lett. **50**, 682 (1983).

[13] P. H. Diamond and Y. B. Kim, Phys. Fluids B **3**, 1626 (1991).

[14] J. F. Drake, J. Finn, P. Guzdar, V. Shapiro, V. Shevchenko, F. Waelbroeck, A. B. Hassam, C. S. Liu, and R. Z. Sagdeev, Phys. Fluids B **4**, 488 (1992).

[15] T. E. Stringer, Phys. Rev. Lett. **22**, 770 (1969).

[16] N. K. Winsor, J. L. Johnson, and J. M. Dawson, J. Comput. Phys. **6**, 430 (1970).

[17] A. B. Hassam, T. N. Antonsen, Jr., J. F. Drake, and C. S. Liu, Phys. Rev. Lett. **66**, 309 (1991).

[18] A. B. Hassam and J. F. Drake, Phys. Fluids B **5**, 4022 (1993).

[19] A. Hasegawa and M. Wakatani, Phys. Rev. Lett. **59**, 1581 (1987).

[20] D. Biskamp, A. Zeiler, Phys. Rev. Lett. **74**, 706 (1995).

[21] P. N. Guzdar, L. Chen, P. K. Kaw, and C. Oberman, Phys. Rev. Lett. **40**, 1566 (1978).

[22] D. Biskamp and M. Walter, Phys. Lett. **109 A**, 34 (1985).

[23] B. D. Scott, Phys. Rev. Lett. **65**, 3289 (1990); B. D. Scott, Phys. Fluids B **3**, 51 (1991); B. D. Scott, Phys. Fluids B **4**, 2468 (1992).

[24] ASDEX Team, Nucl. Fusion **29**, 1959 (1989).

# A Numerical Algorithms

Our numerical simulations are based on the dimensionless equations in field aligned coordinates Eqs. (15)-(17). Since we neglect the radial change of the equilibrium density (only the density *gradient* is retained) there is no explicit $x$ dependence in the equations. The absence of explicit $x$ dependence allows us to use periodic boundary conditions in this direction, thus avoiding profile flattening which can artificially reduce the transport rate. In addition, dissipation is $x$-independent (unlike in a grid based on the untwisted coordinate system) so that the radial correlation lengths are not linked to the grid.

On the other hand, the field aligned coordinates introduce a new problem. As a bundle of flux at a particular $z$ location is mapped down a field line it is stretched along $y$ and compressed along $x$. Thus, the coordinate system becomes extremely distorted with respect to the real system as the system is mapped along $z$. It then becomes very difficult to correctly calculate physical disturbances without introducing an excessively fine radial grid. For example, in the twisted system a disturbance which is $x$ independent in the physical system has $k_x = [2\pi\hat{s}(z - z_0)/L_z]k_y$ in the

flux tube system (see Eq. (10)) so that $k_x \gg k_y$ when $\hat{s} \sim 1$ and $|z - z_0| > L_z$. To avoid this difficulty, we split the flux tube into several boxes in $z$ direction and choose for each box an individual $z_0$ located at the center of the box. If $f^{(1)}$ and $f^{(2)}$ represent the same physical quantity but in the representation of different boxes they must satisfy the matching condition

$$f^{(1)}(x, y, z^*) = f^{(2)}(x, y + 2\pi\hat{s}(z_0^{(1)} - z_0^{(2)})(x - x_a), z^*) \tag{24}$$

at the boundary $z^*$ between the two boxes ($x_a$ denotes an arbitrary reference flux surface). Since radial periodicity must be satisfied in both boxes simultaneously we obtain the additional condition

$$2\pi\hat{s}(z_0^{(1)} - z_0^{(2)})L_x = mL_y \tag{25}$$

which relates the box lengths in $x$ and $y$ direction according to the arbitrary integer number $m$.

Looking for an adequate numerical scheme to solve Eqs. (15)-(17), we notice first that the parallel direction $z$ has to be treated in configuration space since the flux tube must be split into boxes which need to be matched together by a transformation. Hence periodic boundaries are not appropriate. To avoid a severe restriction of the time step the parallel diffusion terms in Eqs. (15) and (16) must be solved implicitely. Since in the vorticity equation $\nabla_\perp^2\phi$ is advanced in time and not $\phi$, the implicit treatment of the parallel diffusion requires a simultaneous solution of the Poisson equation which determines $\phi$. The easiest way to do this is by fourier transforming the equations in $x$ and $y$ which finally leads to the following linear system

$$k_\perp^2\phi_i - \Delta t\frac{h_{i+1} - 2h_i + h_{i-1}}{\Delta z^2} = b_i^\phi \tag{26}$$

$$n + \Delta t\epsilon_n\alpha\frac{h_{i+1} - 2h_i + h_{i-1}}{\Delta z^2} = b_i^n \tag{27}$$

with $i$ labeling the grid points in $z$ direction. This linear system is solved either by a block tridiagonal solver or by reducing the set of equations to a linear system for $h$

$$h - \Delta t\left(\frac{1}{k_\perp^2} + \epsilon_n\alpha^2\right)\frac{h_{i+1} - 2h_i + h_{i-1}}{\Delta z^2} = \frac{b_i^\phi}{k_\perp^2} - \alpha b_i^n \tag{28}$$

which is treated by a standard tridiagonal solver. Afterwards $n$ is computed by inserting $h$ into Eq. (27) and $\phi$ by using the relation $h = \phi - \alpha n$.

We developed two independent different codes to solve the set of equations in order to check the influence of the numerical treatment and the correctness of our codes. The first code follows the numerical scheme which is described in Ref. [1] but treats the parallel diffusion implicitely according to Eq. (28). For all remaining terms a trapezoidal leapfrog algorithm is used as described in Ref. [1]. The nonlinearities due to the $E \times B$ convection are evaluated to fourth order in configuration space.

The spectrum is cut at high mode numbers by a special velocity dependent nonlinear damping which is also described in more detail in Ref. [1].

The second code is a pseudospectral code in the poloidal plane. This allows us to introduce a $\nabla_\perp^6$ hyperviscosity which is solved exactly, thus avoiding any time step restriction due to numerical stability. All remaining linear terms are treated by a Crank-Nicholson scheme. The nonlinear convolutions are computed by multiplication in configuration space with time stepping according to the usual leapfrog scheme. In addition to the perpendicular damping a small parallel diffusion is included. The complete numerical equations are

$$k_\perp^2 \phi_z^{t+1} - \Delta t \left[ \hat{C} n_z^{t+1} + \frac{h_{z+1}^{t+1} - 2h_z^{t+1} + h_{z-1}^{t+1}}{\Delta z^2} \right] =$$

$$= \left\{ k_\perp^2 \phi_z^{t-1} + \Delta t \left[ \hat{C} n_z^{t-1} + \frac{h_{z+1}^{t-1} - 2h_z^{t-1} + h_{z-1}^{t-1}}{\Delta z^2} \right] \right\} \mathrm{e}^{-2(D^\phi k_\perp^2 + \kappa k_{x,y}^6)\Delta t} -$$

$$2\Delta t \tilde{A}_\phi^t \mathrm{e}^{-(D^\phi k_\perp^2 + \kappa k_{x,y}^6)\Delta t},$$

$$n_z^{t+1} + \Delta t \left[ i k_y \phi_z^{t+1} - \epsilon_n \hat{C} h_z^{t+1} + \epsilon_n \alpha \frac{h_{z+1}^{t+1} - 2h_z^{t+1} + h_{z-1}^{t+1}}{\Delta z^2} \right] =$$

$$\left\{ n_z^{t-1} - \Delta t \left[ i k_y \phi_z^{t-1} - \epsilon_n \hat{C} h_z^{t-1} + \epsilon_n \alpha \frac{h_{z+1}^{t-1} - 2h_z^{t-1} + h_{z-1}^{t-1}}{\Delta z^2} \right] - \Delta t \gamma \frac{v_{z+1}^t - v_{z-1}^t}{\Delta z} \right\} \cdot$$

$$\cdot \mathrm{e}^{-2(D^n k_\perp^2 + \kappa k_{x,y}^6)\Delta t} + 2\Delta t \tilde{A}_n^t \mathrm{e}^{-(D^n k_\perp^2 + \kappa k_{x,y}^6)\Delta t},$$

$$v_z^{t+1} = \left\{ v_z^t - \gamma \Delta t \frac{n_{z-1}^{t,t+1} - n_{z+1}^{t,t+1}}{2\Delta z} + \Delta t \tilde{A}_v^t \right\} \mathrm{e}^{-\kappa k_{x,y}^6 \Delta t},$$

with $\tilde{A}_\phi$, $\tilde{A}_n$, and $\tilde{A}_v$ denoting the convective nonlinearities and

$$\hat{C} = [\cos(2\pi z\,\Delta z) + 2\pi \hat{s}(z\,\Delta z - z_0)\sin(2\pi z\,\Delta z) - \epsilon]\, i k_y + \sin(2\pi z\,\Delta z) i k_x,$$

$$k_\perp^2 = [k_x + 2\pi \hat{s}(z\,\Delta z - z_0) k_y]^2 + k_y^2, \quad k_{x,y}^2 = k_x^2 + k_y^2, \quad h_z^t = \phi_z^t - \alpha n_z^t.$$

The dissipation terms in $z$ direction have been dropped. The matching between different boxes in $z$ direction is done by explicitely using the values of the adjacent box after transforming according to Eq. (24). To ensure numerical stability we use the most recent values in the adjacent box, hence the values at time $t+1$ if the box has been advanced already. To avoid boundary effects we close the flux tube in $z$ direction according to the same matching procedure.